

Beyond the Label Itself: Latent Labels Enhance Semi-supervised Point Cloud Panoptic Segmentation

Yujun Chen^{1,2,*}, Xin Tan^{1,2,*}, Zhizhong Zhang^{1,2,†}, Yanyun Qu³, Yuan Xie^{1,2}

¹School of Computer Science and Technology, East China Normal University

²Chongqing Institute, East China Normal University

³School of Information Science and Engineering, Xiamen University

51215901065@stu.ecnu.edu.cn, {xtan, zzzhang, yxie}@cs.ecnu.edu.cn, yyqu@xmu.edu.cn

Abstract

As the exorbitant expense of labeling autopilot datasets and the growing trend of utilizing unlabeled data, semi-supervised segmentation on point clouds becomes increasingly imperative. Intuitively, finding out more “unspoken words” (i.e., latent instance information) beyond the label itself should be helpful to improve performance. In this paper, we discover two types of latent labels behind the displayed label embedded in LiDAR and image data. First, in the LiDAR Branch, we propose a novel augmentation, Cylinder-Mix, which is able to augment more yet reliable samples for training. Second, in the Image Branch, we propose the Instance Position-scale Learning (IPSL) Module to learn and fuse the information of instance position and scale, which is from a 2D pre-trained detector and a type of latent label obtained from 3D to 2D projection. Finally, the two latent labels are embedded into the multi-modal panoptic segmentation network. The ablation of the IPSL module demonstrates its robust adaptability, and the experiments evaluated on SemanticKITTI and nuScenes demonstrate that our model outperforms the state-of-the-art method, LaserMix.

Introduction

Point clouds, with richer visual and geometric information, have played an increasingly significant role in perception tasks (Roriz, Cabral, and Gomes 2021; Triess et al. 2021). Given its extensive potential, point cloud panoptic segmentation, unifying instance and semantic segmentation, has been applied in various fields, such as autonomous driving, robotics, and industrial manufacturing (Geiger, Lenz, and Urtasun 2012; Fernandes et al. 2021; Wang and Kim 2019).

However, it is exhausting to annotate point cloud data, which prohibitively restricts its potential applications (Hu et al. 2022; Unal, Dai, and Van Gool 2022; Xu and Lee 2020). Hence, it is highly demanded to utilize less point data to achieve better performance. Nowadays, images play a crucial role in point cloud segmentation since they are cost-effective (Cui et al. 2021; Li and Lee 2021). In addition, with the larger number of unlabeled point cloud data collected, the trend towards semi-supervision is prevalent (Sindhwani,

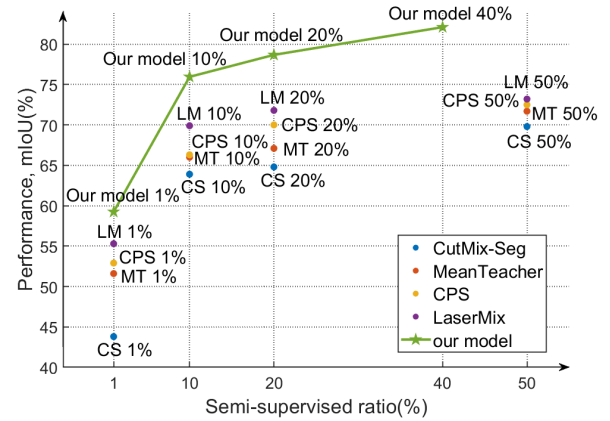


Figure 1: Segmentation quality at various Semi-supervised ratios. Our model outperforms all other methods in mIoU.

Niyogi, and Belkin 2005; You et al. 2022). Thus, in this paper, we pay attention to semi-supervised multi-modal point cloud (panoptic) segmentation (SMPS).

We have observed two major limitations in the previous SMPS methods. First, due to the limited ground-truth data, the preceding semi-supervised (SS) models generated pseudo-labels as ground-truth for training (Kong et al. 2023; Park et al. 2022). Nevertheless, such pseudo-labels are sometimes unreliable and of poor quality when the network is not fully trained. Second, for the 3D-2D cross-modal processing, previous multi-modal point cloud models (Liu et al. 2022; Liang et al. 2022) treat all pixels equally without leveraging sufficient image-level information (e.g., size and boundary), despite the fact that images have a superior ability to detect and locate objects, which even outperforms point clouds in certain cases (Park et al. 2022).

According to the above discussions, we argue that the information contained in point cloud labels is not only as superficial as the displayed label itself but also encompasses some latent labels beneath the surface. Hence, it is a feasible solution to explore unspoken words (i.e., latent labels) to address the two issues. Specifically, for the first, since only given labeled data is reliable and completely correct, 1) *can we exploit self-information among labeled point clouds to construct other reliable and diverse labels?* For the second

*These authors contributed equally.

†Corresponding author.

one, the existing 3D instance labels can be projected onto the image as a form of weak 2D annotations, which indicate the instances’ position and scale. Therefore, 2) *can we utilize these weak annotations from 3D-2D self-information to improve the network segmentation performance?*

In this paper, we propose to address the limitations by discovering more latent labels. As illustrated in Figure 1, our method significantly surpasses previous semi-supervised point cloud segmentation ones.

First, we propose a novel data augmentation method, Cylinder-Mix, to obtain reliable and diverse samples for training. Specifically, to exploit self-information within limited data, It performs interleaved mixing for labeled point clouds based on cylinder voxels. This kind of mix strategy does not require other annotations, and the obtained labels are all as accurate as the human-annotated ones.

Second, Instance Position-Scale Learning (IPSL) Module is proposed to learn the instance information of position and boundary on images. In this module, latent labels from 3D-2D self-information, the instance boxes, are obtained through LiDAR-to-camera projection. Subsequently, inspired by interactive image segmentation (IIS) (Ramadan, Lachqar, and Tairi 2020; Lin et al. 2020), weak interactive annotation (e.g., the bounding box with location and boundary information) leads the network to pay more attention to the highlighted object. Hence, the boxes, which serve as interactive annotations, are encoded into heatmaps to indicate positions and scales, and then fused to the 2D backbone. This way, these latent labels from 3D-2D projection highlight the instances so as to improve segmentation.

Furthermore, our experiments demonstrate the adaptability and versatility of the IPSL module, as it still works well whether it fuses instance boxes from a trained detector or masks from a large model (e.g., SAM (Kirillov et al. 2023), and Grounded-Segment-Anything (Contributors 2023)). Additionally, to our best knowledge, our model is the first multi-modal model applying the semi-supervised setting to solve point cloud panoptic segmentation.

In summary, our contributions are summarized as follows:

- We explore latent labels from self-information on both point clouds and images, without requiring any extra labels, to enhance network segmentation performance. Surprisingly, our model finally achieves state-of-the-art performance on semi-supervised semantic segmentation, surpassing the previous best method, LaserMix.
- We propose a novel data augmentation technique, Cylinder-Mix, that could obtain reliable and diverse labels, as accurate as the given ground-truth, within limited labeled data for semi-supervised training.
- We propose the Instance Position-scale Learning (IPSL) Module to fuse latent annotations from 3D-2D self-information. The obtained latent labels, instance boxes, are utilized to provide position and scale explicitly.

Related Work

Fully-supervised Point Cloud Segmentation. In recent years, the efficiency of point cloud segmentation has been enhanced mainly by 3D perspective feature extraction

(Zhou, Zhang, and Foroosh 2021; Li et al. 2022a; Fong et al. 2022; Qi et al. 2017) and multi-modal fusion (Liu et al. 2022; Liang et al. 2022; Zhang et al. 2023; Tan et al. 2023; Liu et al. 2021). Cylinder-3D (Zhu et al. 2021) proposes a novel voxelization approach for the geometric properties of the point cloud, while Panoptic-PolarNet (Zhou, Zhang, and Foroosh 2021) utilizes the Bird’s Eye View (BEV) feature for segmentation and clustering, which not only realizes the panoramic segmentation, but also avoids the occlusion issue between instances. However, the 2D image branch has been somewhat neglected, leaving the network far from better performance during semi-supervised tasks. Although BEVfusion (Liu et al. 2022) combines images, it treats all pixels equally without using instance information. Distinctively, we do not only fuse the image features but also focus more on the instance position and boundary of the image, so as to implicitly enhance the performance of the SS segmentation network in the process of multi-modal fusion.

Semi-Supervised Point Cloud Methods. Several methods for indoor scenes have been proposed. SSPC-Net (Cheng et al. 2021) utilizes pseudo-label propagation through superpixel segmentation, while Jiang et al. (2021) applies Guided Point Contrastive Loss to semi-supervised indoor datasets. However, such methods are unable to effectively handle large-scale real-world datasets, such as SemanticKITTI and nuScenes, due to their large number of points and objects. For methods on real-world datasets, LaserMix (Kong et al. 2023), adapting Mean Teacher (Tarvainen and Valpola 2017) architecture to SS point segmentation, proposes a new circular mixture data augmentation. However, the generated samples from LaserMix can be unreliable due to the mixture of unlabeled data since the network is not always well-trained. DetMatch (Park et al. 2022) applies the Mean Teacher architecture to detection tasks, but lacks sufficient adaptability for panoptic segmentation like Panoptic-PolarNet. In contrast, our proposed data augmentation, Cylinder-Mix, not only generates reliable and diverse labels from limited labeled data for training but also inherits the excellent feature extraction capability of Cylinder3D, thus making it adaptable for semi-supervised panoptic segmentation tasks on the real-world dataset.

Preliminaries

Problem Setting. Semi-supervision usually uses the whole points of partial samples or frames. We adopt a sampling method of selecting frames with fixed intervals, which is the same as Kong et al. (2023). In this paper, we have respectively selected 40%, 20%, 10%, and 1% point cloud frames with point-wise labels for training.

Symbols. We use $\mathbf{P} = \{(x, y, z, b)\}_{n=1}^N$ to denote a 3D LiDAR point cloud, with the RGB image(s) $\mathbf{I} = \{I \in \mathbb{R}^{H \times W \times 3}\}_v$, where (x, y, z) indicates the spatial coordinates, b is the brightness of each point, N and v are respectively the number of points and camera views. Besides, there are point-wise semantic and panoptic labels $\mathbf{L} = \{l_{sem}, l_{inst}\}_{n=1}^N$, $l_{sem} \in [1, 2, 3, \dots, C]$, where C is the number of semantic categories. Therefore, the dataset could be represented as $\mathbb{P} = \{\mathbf{P}, \mathbf{I}, \mathbf{L}\}_{i=1}^M$ with M frames. During training, the dataset is divided into labeled and unlabeled

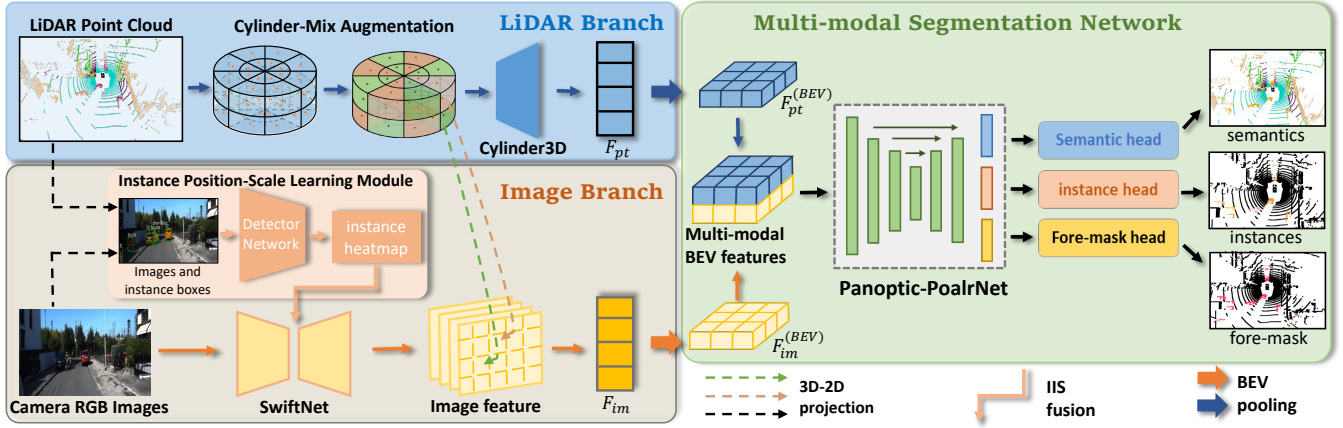


Figure 2: The framework of our model. Our model is composed of three parts. LiDAR Branch, on the 3D point cloud branch, gets better 3D features through self-supervised augmentation, called Cylinder-Mix, while Image Branch improves the 2D backbone via fusion of instance position and scale information. After that, both cross-modal features will be fused to the BEV feature, following Multi-modal Segmentation Network to extract features and get point-wise labels in the end.

parts, denoted by the superscript l and u , respectively. For example, \mathbf{P}^u means unlabeled points of the dataset.

Method

As shown in Figure 2, LiDAR Branch, given the labeled point clouds, outputs point-wise features through Cylinder-Mix augmentation and Cylinder3D (Zhu et al. 2021) extractor network. On Image Branch, the proposed Instance Position-Scale Learning (IPSL) module outputs instance heatmaps. To this end, a detector, supervised by the 3D-2D projected instance boxes, is introduced into this module to predict boxes. Ultimately, the instance heatmaps are fused into the backbone, SwiftNet (Orsic et al. 2019), so that the pixel features corresponding to the 3D points on the image are generated. Then, the features from two branches are processed by Multi-modal Segmentation Network, which consists of the BEV-pooling (Li et al. 2022b) and Panoptic-PolarNet (Zhou, Zhang, and Foroosh 2021). Finally, we get semantic and instance predictions for each point via multi-heads and clustering. Additionally, self-training is utilized for unsupervised data, similar to Xu et al. (2021).

Training LiDAR Branch

Pipeline The objective of this branch is to learn well-behaved feature comprehension of Cylinder3D. It also employs Cylinder-Mix for achieving more latent samples and self-supervised enhancement.

As shown in the blue part of Figure 2, LiDAR Branch learns point-wise features with the input of a point cloud \mathbf{P} . Firstly, it voxelized the points into cylindrical voxels with the grid size of $[G_x, G_y, G_z]$ where G_x is the number of blocks of voxels to be split along the X-axis, so as to G_y, G_z . This way we get the grid index (v_x, v_y, v_z) that denotes which cylinder-voxel the point (x, y, z) belongs to. Secondly, it applies our proposed Cylinder-Mix to increase the diversity of the point clouds within the limited data.

The augmented points \mathbf{P}_{mix} are fed into the MLP-based feature extractor of Cylinder3D, thus getting point-wise features $F_{pt} \in \mathbb{R}^{N \times C_b}$. Finally, through the grid index of points and BEV pooling, we aggregate F_{pt} into LiDAR BEV features $F_{pt}^{(BEV)}$ with the size of $G_x \times G_y \times G_z \times C_b$, where C_b is the number of channels of the BEV feature. When pooling the voxel at position (v_x, v_y, v_z) , its BEV feature is the maximum of point features $F_{pt}(p)$ within the point set $\mathbf{S}_{(x,y,z)}$ in which all points belong to this voxel.

$$F_{pt}^{(BEV)}(v_x, v_y, v_z) = \max_{p \in \mathbf{S}_{(x,y,z)}} F_{pt}(p). \quad (1)$$

Cylinder-Mix Augmentation To obtain more data for network training, we propose a point cloud mixture data augmentation, Cylinder-Mix. It, without additional annotations, provides more diverse point clouds for network training and adapts well to the feature extraction of Cylinder3D.

To fully mix the point cloud samples, we perform an interleaved mixing as figure 3. This means that for a certain block region of the mixed point cloud, its surrounding regions (i.e., above, below, to the left, and to the right) all come from another different point cloud.

Given the point cloud samples $\mathbf{P}_1, \mathbf{P}_2$ and their cylinder voxel index of each point $V = \{(v_x, v_y, v_z)\}_{n=1}^N$ with the grid size of $[G_x, G_y, G_z]$, we first divide the two point clouds into mixture regions with the size $[R_x, R_y, R_z]$ along each x, y and z axis. For example, the region size of the mixture shown in Figure 3 is $[8, 1, 2]$. To mix them, we calculate the (r_x, r_y, r_z) of each point, where $r_x \in \{0, 1, 2, \dots, R_x - 1\}$ represents the index number of the mixture region, which point belongs to the x axis, similarly for r_y and r_z .

$$r_k = \lfloor v_k / G_k \times R_k \rfloor, \quad (k = x, y, z). \quad (2)$$

For interlaced mixing, the two point clouds $\mathbf{P}_1, \mathbf{P}_2$ are mixed according to index-judgment as the following:

$$\delta(r_k) = \begin{cases} \text{True}, & \text{if } \text{mod}(r_k, 2) = 0 \\ \text{False}, & \text{if } \text{mod}(r_k, 2) = 1 \end{cases}, (k = x, y, z). \quad (3)$$

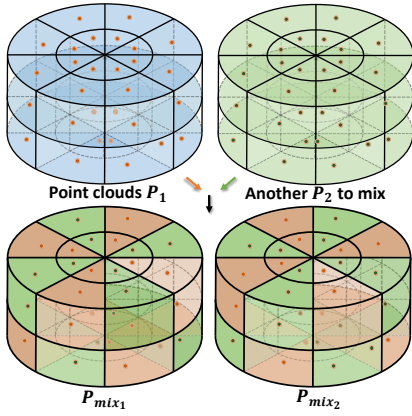


Figure 3: Sketch map of Cylinder-Mix.

$$\mathcal{J}(x, y, z) = \neg(\delta(r_x) \oplus \delta(r_y)) \oplus \delta(r_z). \quad (4)$$

In equation 4, \neg and \oplus indicate logical negation and xor, respectively. $\mathcal{J}_1(x, y, z)$ is a judgment function for judging whether the point at (x, y, z) will be mixed into the point clouds \mathbf{P}_{mix_1} . To get the another mixed point clouds \mathbf{P}_{mix_2} , the index-judgment function $\mathcal{J}_2 = \neg\mathcal{J}_1$.

$$\mathbf{P}_{mix_1} = \mathbf{P}_1[\mathcal{J}_1(\mathbf{P}_1)] \cup \mathbf{P}_2[\mathcal{J}_1(\mathbf{P}_2)]. \quad (5)$$

On this basis, we get mixed points by equation 5, as shown in Figure 3. Attention that for the mixed point cloud from \mathbf{P}_1 and \mathbf{P}_2 , its Image Branch should perform feature extraction and projection for camera images \mathbf{I}_1 and \mathbf{I}_2 , respectively. In addition, consistently training with mixed data can potentially cause the model distribution to deviate from that of training with original data. Hence, we set p_{cylmix} , the probability of using Cylinder-Mix, to control this augmentation.

Training Image Branch

Pipeline Image Branch is aimed at extracting image features and learning instance information from some weak labels. As shown in the orange part of Figure 2, Image Branch consists mainly of two parts: the backbone network (SwiftNet (Orsic et al. 2019) in our experiment) and the Instance Position-scale Learning (IPSL) Module. Further details on this module will be presented in the next section. Given the corresponding images of the point cloud, this branch is expected to output camera BEV features.

With the input images \mathbf{I} of point clouds and the fusion of the instance information from the IPSL Module, SwiftNet encodes initial pixel-wise features F_{im} . To obtain camera BEV features, we employ the LiDAR-to-camera projection, through camera intrinsic parameters and vehicle parameters, to project the point $p = (x, y, z)$ onto the camera coordinate system $q = (h, w)$. We obtain a set of matched pairs mapping $\mathbf{M} = \{p, q\}$ between 3D points and 2D pixels. Subsequently, we perform BEV pooling on the matched pixel features to get the camera BEV feature. Its value on (v_x, v_y, v_z) is the maximum of pixel features $F_{im}(q)$, where q is in set $\mathbf{M}_{(v_x, v_y, v_z)}$ and the matched point belongs to its voxel.

$$F_{im}^{(BEV)}(v_x, v_y, v_z) = \max_{(p, q) \in \mathbf{M}_{(v_x, v_y, v_z)}} F_{im}(q). \quad (6)$$

Instance Position-scale Learning Module The Instance Position-scale Learning Module is aimed to utilize weak labels on images to provide instance information for improving point cloud segmentation. Inspired by interactive image segmentation (IIS) (Sofiiuk, Petrov, and Konushin 2022), images with weak annotations, such as a point indicating the center of an object, make the model pay more attention to the annotated objects. Next, we will introduce how to generate and utilize weak annotations.

Initially, to train with weak labels, it is necessary to get the latent ground-truth through the instance labels of points and LiDAR-to-camera projection. This involves matching and projecting the 3D points onto 2D pixels. For a specific object with the instance label y_{inst} , its box can be enclosed by the maximum and minimum values of pixel coordinates (h, w) from projected points of this instance. Subsequently, we preserve these box labels and use them as targets to train the Detection Network. The Detection Network is an offline network, and it is convenient to adopt any detection backbone. In our experiment, we directly select the detection model from MMDetection (Chen et al. 2019).

In this way, the module predicts the instance bounding boxes of cameras through the trained Detection Network. Since these boxes are in 2D coordinates, we convert them into instance heatmaps using the following equation:

$$d_q(m, n) = \sqrt{(h - m)^2 + (w - n)^2}, \quad (7)$$

$$H_q(m, n) = \begin{cases} \exp(-2d_{mn}^2/R^2) & d_{mn} \leq R \\ 0 & d_{mn} > R \end{cases}, \quad (8)$$

where $d_q(m, n)$ is the distance on the image coordinate system between pixel (m, n) and $q = (h, w)$. The H_q is a Gaussian-based heatmap of a box angular or box center point q , with the radius of R .

In implementation, the heatmap of an instance is gathered by its 4 box angular points q_1, q_2, q_3, q_4 and its center point q_{cen} of the box. $R = 5$ for each of the 4 corners, while for its center, R is determined by the product of the instance width and the percentage P_{center} . Here, instance width is the minimum value between the box length and width. We set $P_{center} = 1/4$ as the default. To ascertain the optimal configuration of these parameters, we conduct comprehensive ablation experiments, as detailed in the Appendix.

With stacking the heatmaps $[H_{q_1}, H_{q_2}, H_{q_3}, H_{q_4}, H_{q_{cen}}]$ and maximizing at the stacked dimension, we get the instance heatmap of the box. Furthermore, for the camera image from view v , its instances heatmap is the maximum of Gaussian heatmap of each instance.

Finally, referring to the fusion block of IIS (Sofiiuk, Petrov, and Konushin 2022), these heatmaps and images along with each camera view, are fused together on intermediate features. with camera images I . As shown in equation 9, images I and heatmaps H are aligned through their respective mapping heads ψ_H and ψ_I , 2D convolution with the number of output channels 64. And then they are summed to obtain fused intermediate features F_{IH} and fed into the backbone of Image Branch for further extraction.

$$F_{IH} = \psi_H(\mathcal{H}) + \psi_I(I). \quad (9)$$

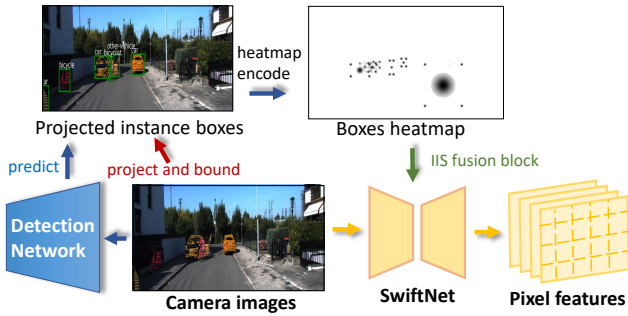


Figure 4: sketch map of IPSL Module on Image Branch.

Instance Heatmap from SAM Masks. There is another method to obtain instance heatmaps. Due to the development of large models such as CLIP (Radford et al. 2021), SAM (Kirillov et al. 2023), and Grounded-Segment-Anything (Contributors 2023), instance masks are still available even without fine-tuning autopilot camera images. Therefore, through zero-shot segmentation by Grounded-Segment-Anything, we get n_i instance masks $Mask$ and their scores Sco on an image. The instance heatmap could be the weighted sum of all those masks.

$$\mathcal{H} = \sum_{i=1}^{n_i} Mask_i * Sco_i. \quad (10)$$

Multi-modal Segmentation Network

It is expected to get panoptic results with the backbone of Panoptic-Polarnet (Zhou, Zhang, and Foroosh 2021) and multi-heads.

$$F^{(BEV)} = \mathcal{L}(F_{pt}^{(BEV)} \otimes F_{im}^{(BEV)}). \quad (11)$$

The multi-modal BEV features are obtained with LiDAR and Camera ones through equation 11, where \otimes means concatenation along the channel dimension and \mathcal{L} represents the linear fully connected layer to compress the feature dimension. $F^{(BEV)}$ is input into the Multi-modal Segmentation Network. To achieve panoramic segmentation, multi-heads include semantic and instance heads, and the latter is responsible for predicting heatmaps of offset and center. Moreover, a fore-mask head is added for *thing* classes perception. We utilize the above mask and heatmaps, based on predicted semantic labels, to cluster and ultimately identify instances.

Segmentation Loss. The loss of segmentation \mathcal{L}_{seg} , besides semantic loss and instance losses of the panoptic network, we also added foreground mask loss. With predicted logits of each point on semantic head and ground-truth, we could get semantic loss \mathcal{L}_{sem} by **cross-entropy** loss. For instance head, we use **MSE** loss (\mathcal{L}_{hm}) and **L1 Loss** (\mathcal{L}_{os}) to fit the center heatmap of instances $\mathbf{hm} \in \mathbb{R}^{H \times W \times 1}$ and offset of each point $\mathbf{os} \in \mathbb{R}^{H \times W \times 2}$. For fore-mask head, we use **MSE** loss (\mathcal{L}_{fm}) to fit foreground mask $\mathbf{fm} \in \mathbb{R}^{H \times W \times 1}$, in which 1 and 0 denote *thing* and background classes. The final loss with coefficients is

$$\mathcal{L}_{seg} = \mathcal{L}_{sem} + \mu_{hm}\mathcal{L}_{hm} + \mu_{os}\mathcal{L}_{os} + \mu_{fm}\mathcal{L}_{fm}. \quad (12)$$

Self-Training

First, we train our model with labeled data and loss as equation 12, which is called **pretraining**. Second, pseudo labels of unlabeled data are **estimated** with the pretrained model. Third, after loading with the parameter of pretraining, we will **retrain** model with labeled and estimated data. Noted that with the decrease in the amount of labeled data during pretraining, the lower semi-supervised percentage, the more epochs are required. And the specific epoch of each setting is given in the section on Experiments.

Experiments

Dataset and Metrics

SemanticKITTI (Behley, Milioto, and Stachniss 2021) contains 10 (1/11) training (validation/testing) sequences and totally 43551 LiDAR scans with a 64-beam LiDAR sensor, as well as binocular camera images of each scan additionally. There are point-wise panoptic annotations with 8 *thing* class and 12 *stuff* class labels with instance labels.

nuScenes (Caesar et al. 2020) is a large-scale autopilot dataset with various urban scenes and a 32-beam LiDAR sensor. It totally contains 1000 driving scenes of 20s duration and point-wise panoptic annotations, with 16 semantic classes, 10 of which are *thing* classes. For the camera, there are 6 views of images per scan.

Metrics. Typically, panoptic quality (PQ) is used to evaluate panoptic segmentation as Kirillov et al. (2019). And mean IoU (mIoU) reflects the quality of semantic segmentation. For the detector on IPSL Module, average precision (AP) is used to measure the quality of predicted boxes.

Implementation Details

Our baseline comprises an image encoder (SwiftNet), a LiDAR encoder (Cylinder3D), and a decoder (Panoptic-PolarNet). It can be comprehended as the combination of section of *Image Branch and LiDAR Branch pipeline*, as well as *Multi-modal Segmentation Network*, with the exclusion of the description of the proposed IPSL module and Cylinder-Mix. Additionally, the instance augmentation of PUPS (Su et al. 2023) is applied.

Implementation Default settings unless ablation. In IPSL Module, the radius of Gaussian heatmaps $R = 5$, percentage of scale to the center $P_{center} = 1/4$. For Cylinder-Mix, the region size $[R_x, R_y, R_z] = [4, 4, 2]$, the probability $p_{cylmix} = 25\%$. For the weight of each term in loss in \mathcal{L}_{seg} , $\mu_{hm} = 100, \mu_{os} = 10, \mu_{fm} = 1$. More *Implementation Details* of Detection Network and point cloud segmentation network are in the Appendix.

Experimental Results

Results of Detection Network We utilize Faster R-CNN with ResNet-101 (He et al. 2016) to train the detector. The result mAP on the fully nuScenes dataset is only 31.2%. However, these predicted instance boxes, acting as weak labels, can enhance point segmentation even without high precision. See the detailed class-wise mIoU in the Appendix.

	Method	nuScenes					SemanticKITTI				
		1%	10%	20%	50%*	100%	1%	10%	20%	50%*	100%
mIoU	CutMix-Seg (BMVC2020)	43.8	63.9	64.8	69.8	/	37.4	54.3	56.6	57.6	/
	MeanTeacher (NIPS2019)	51.6	66.0	67.1	71.7	/	45.5	57.1	59.2	60.0	/
	CBST (ECCV2018)	53.0	66.5	69.6	71.6	/	48.8	58.3	59.4	59.7	/
	CPS (CVPR2021)	52.9	66.3	70.0	72.5	/	46.7	58.7	59.6	60.5	/
	LaserMix (CVPR2023)	55.3	69.9	71.8	73.2	/	50.6	60.0	61.9	62.3	/
	baseline	56.2	72.7	77.0	79.8*	80.7	51.2	61.8	62.6	64.7*	64.2
	our model	59.1	76.0	78.7	80.5*	82.1	52.8	64.8	64.9	65.9*	65.3
$\Delta \uparrow$	+2.9	+3.3	+1.7	+0.7	+1.4	+1.6	+3.0	+2.3	+1.2	+1.1	
PQ	baseline	47.0	67.8	71.9	75.5*	77.6	46.5	57.0	59.3	60.4*	59.8
	our model	49.8	70.9	75.6	77.2*	78.6	49.0	59.9	60.8	61.2*	60.8
	$\Delta \uparrow$	+2.8	+3.1	+3.7	+1.7	+1.0	+2.5	+2.9	+1.5	+0.8	+1.0

Table 1: Segmentation results compared with other semi-supervised methods on validation set of nuScenes and SemanticKITTI. The symbol * in the table denotes semi-supervised results at a ratio of 40%, distinguishing them from other methods at 50%.

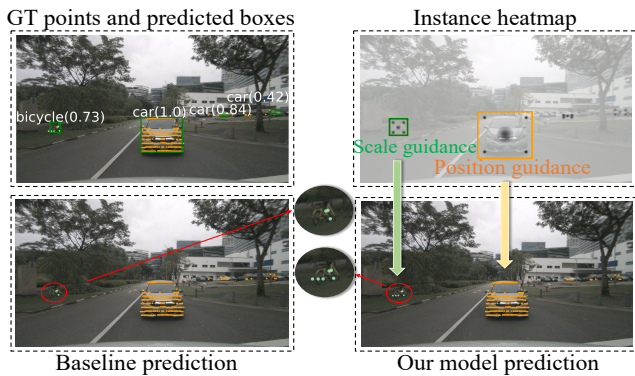


Figure 5: Guidance on instance position and scale. After the detector predicts instance boxes, our model generates instance heatmaps (top-right image) to provide position and scale information. See the bicycle (better zoom in), it achieves better segmentation compared to the baseline.

Results of Panoptic Segmentation Firstly, we present the **Quantitative Results** as Table 1. It shows segmentation results on the validation set. As there are limited panoramic segmentation methods available for SS methods, we compare our model with previous methods (French et al. 2019; Tarvainen and Valpola 2017; Zou et al. 2018; Chen et al. 2021; Kong et al. 2023) with semantic segmentation metrics (mIoU, %) and attach our panoptic segmentation metrics (PQ, %). Eventually, our model outperforms the previous top, LaserMix, and attains state-of-the-art semantic results.

Our model excels in the semi-supervised setting, as it exhibits superior performance when given a smaller amount of labeled data. On nuScenes and SemanticKITTI at 10%, the model achieves 3.1% and 2.9% improvement on PQ and 3.3% and 3.0% improvement on mIoU, respectively, compared to the baseline. Moreover, at the setting of 20% labeled data on SemanticKITTI, our model achieves comparable performance to the fully-supervised baseline, and even surpasses that at the setting of 40%.

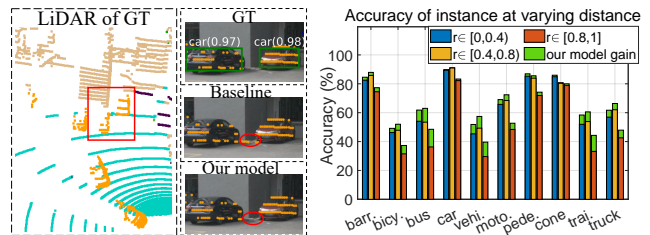


Figure 6: Enhanced performance near the instance boundaries. The left image illustrates the ground-truth and the projected prediction, where our model improves segmentation on the boundaries between instances. The right presents the class-wise classification accuracy. Each set of three bars corresponds to points close, medium, and far from the instance center, based on the distance-to-instance size ratio r_{ds} . The upper part represents the enhancement achieved.

Visualization. Our model excels in **scale and position guidance**. As shown in Figure 5), with the instance heatmaps, our model achieves superior segmentation in terms of instance scale. Moreover, the heatmap position guidance helps alleviate false positives in some small and distant instances. Figure 6 illustrates our model’s superior segmentation on **instance boundary** points. In terms of metrics, the bar graph on the right (representing points distant from the instance center) of each class shows the greatest accuracy increase, suggesting that our model pays more attention to points near the boundaries.

Ablation Studies

Compare with LaserMix For a fair comparison, we compare our model with LaserMix under the same baseline. As demonstrated in Table 2, there are two scenarios: firstly, using LaserMix not only its framework (Mean Teacher) but also its data augmentation simultaneously (baseline + LaserMix), and secondly, employing only the augmentation while keeping other conditions constant (baseline + LaserMix*).

		1%	10%	20%	40%
PQ	baseline	46.5	57.0	59.3	60.4
	baseline+LaserMix	46.0	56.5	59.0	59.7
	baseline+LaserMix*	47.0	58.4	60.0	59.9
	baseline+Cylinder-Mix	49.0	59.9	60.8	61.2
mIoU	baseline	51.2	61.8	62.6	64.7
	baseline+LaserMix	49.7	62.3	63.9	64.8
	baseline+LaserMix*	50.4	64.1	64.7	65.5
	baseline+Cylinder-Mix	52.8	64.8	64.9	65.9

Table 2: Comparison of Cylinder-Mix between LaserMix.

baseline	IPSL	CM	10%	20%	40%
✓			67.8	71.9	75.5
✓	✓		68.4	74.0	76.2
✓		✓	68.5	74.6	76.1
✓	✓	✓	70.9	75.6	77.2

Table 3: Ablation of IPSL and Cylinder-Mix on nuScenes

In the third row of Table 2, LaserMix exhibits improvements at 10% and 20% semi-supervised ratios. Nevertheless, our Cylinder-Mix surpasses it. Second, to further eliminate the framework bias, we exclusively use LaserMix instead of Cylinder-Mix for data augmentation while keeping all other factors unchanged. The third and seventh rows of Table 2 reveal that Cylinder-Mix consistently outperforms LaserMix.

Reliable potential samples. As shown in the 2, the pretrain-retrain approach is employed in LaserMix, where only labeled point clouds are mixed and these samples are reliable. In contrast, the Mean Teacher approach, employed in LaserMix*, mixes labeled and unlabeled points, with pseudos predicted by the Teacher Network. However, these pseudos are unreliable, especially in a low semi-supervised ratio. Both are fundamentally identical, except that the former train has additional and reliable mixed samples derived from labeled point clouds. Experimental results demonstrate that the former outperforms the Mean Teacher approach comprehensively. This indicates that the labels augmented by Cylinder-Mix are reliable and of high quality.

Components Analysis We conduct ablations on the Instance Position-scale Learning (IPSL) Module and Cylinder-Mix (CM) with their default settings.

Ablation on nuScenes. As shown in Table 3, we presented the PQ values with semi-supervised ratios of 10%, 20% and 40%, where ✓ indicates whether IPSL and Cylinder-Mix are used. The results indicate that both modules are effective on the nuScenes dataset. IPSL performed best at a 20% proportion, bringing a 2.1% increase in PQ, while Cylinder-Mix shows a 2.7% increase at the 10% setting. Cylinder-Mix tends to have a greater impact with a smaller amount of data. Moreover, we can draw the conclusion that both the Cylinder-Mix and IPSL module exhibit performance gain on nuScenes dataset.

Ablation on SemanticKITTI is present in the Appendix.

		10%	20%	40%
baseline		67.8	71.9	75.5
mAP of SS-detector		23.8	27.2	28.1
+ IPSL(SS-detector)		70.2	75.1	76.3
+ IPSL(KITTI-detector)		69.9	74.8	76.0
+ IPSL(GSA mask)		70.7	75.3	76.3
+ IPSL(fully detector)		70.9	75.6	77.2

Table 4: Ablation study of IPSL on nuScenes. SS-detector and fully detector are trained with semi-supervised and fully nuScenes, while KITTI-detector from SemanticKITTI.

Instance Position-Scale Learning Module We conduct ablation experiments for the IPSL to demonstrate its **strong generality**, where even when using detectors from different datasets or detectors with slightly lower accuracy on partial datasets, the performance is comparable.

Undemanding Detector. First, IPSL does not require high accuracy from the detector. As shown in Table 4, comparing IPSL(SS-detector) and IPSL(fully detector), the mAP of the detector trained with a partial dataset is slightly lower than that of the fully trained detector by 31.2%. However, their PQ results are comparable.

From Different datasets. Second, IPSL still works with detectors from different datasets. Due to the class-agnostic nature of the heatmap in IPSL, the detector trained on SemanticKITTI can be used to predict boxes for nuScenes images. The similarity between IPSL(KITTI-detector) and IPSL(fully detector) in Table 4 further confirms the universality of the detector of IPSL.

From LLM masks. Third, comparing IPSL (GSA mask) with the baseline and IPSL (fully detector), we observe that utilizing masks predicted by a large model, Ground-Segment-Anything (GSA), remains effective in IPSL. This further validates the generality of the IPSL module and aligns with our initial motivation for designing IPSL.

Fine-grained Analysis of Module Parameters We perform ablations on the parameters of the IPSL module and Cylinder-Mix, including P_{center} for IPSL and p_{cylmix} and region size for Cylinder-Mix, to ensure their rationality. Detailed results and analyses can be found in the Appendix.

Conclusion

In this paper, we exploit the latent labels from the original labels for semi-supervised multi-modal point cloud panoptic segmentation. For LiDAR data, we introduce a novel data augmentation to generate more and reliable point clouds from limited labeled data. For images, we propose the IPSL module to learn and fuse the information of instance position and scale. We compare our approach with other methods and demonstrate the effectiveness and adaptability of our model by applying a large-scale architecture to our proposed module. Our approach provides inspiration for understanding and mining deeper information from LiDAR-Camera data.

Acknowledgments

This work is supported by the National Natural Science Foundation of China (No.62222602, 62302167, U23A20343, 62106075, 62176224,62176092), Development Project of Ministry of Industry and Information Technology (ZTZB-23-990-016), Shanghai Sailing Program under Grant (23YF1410500), Natural Science Foundation of Shanghai (23ZR1420400), Natural Science Foundation of Chongqing (CSTB2023NSCQ-JQX0007, CSTB2023NSCQ-MSX0137), CCF-Tencent Rhino-Bird Young Faculty Open Research Fund (RAGR20230121), CAAI-Huawei MindSpore Open Fund.

References

- Behley, J.; Milioto, A.; and Stachniss, C. 2021. A Benchmark for LiDAR-based Panoptic Segmentation based on KITTI. In *2021 IEEE International Conference on Robotics and Automation (ICRA)*, 13596–13603. IEEE.
- Caesar, H.; Bankiti, V.; Lang, A. H.; Vora, S.; Liong, V. E.; Xu, Q.; Krishnan, A.; Pan, Y.; Baldan, G.; and Beijbom, O. 2020. nuscenes: A multimodal dataset for autonomous driving. In *Proceedings of the IEEE/CVF conference on computer vision and pattern recognition*, 11621–11631.
- Chen, K.; Wang, J.; Pang, J.; Cao, Y.; Xiong, Y.; Li, X.; Sun, S.; Feng, W.; Liu, Z.; Xu, J.; et al. 2019. MMDetection: Open mmlab detection toolbox and benchmark. *arXiv preprint arXiv:1906.07155*.
- Chen, X.; Yuan, Y.; Zeng, G.; and Wang, J. 2021. Semi-supervised semantic segmentation with cross pseudo supervision. In *Proceedings of the IEEE/CVF Conference on Computer Vision and Pattern Recognition*, 2613–2622.
- Cheng, M.; Hui, L.; Xie, J.; and Yang, J. 2021. Spsc-net: Semi-supervised semantic 3d point cloud segmentation network. In *Proceedings of the AAAI conference on artificial intelligence*, volume 35, 1140–1147.
- Contributors, G.-S.-A. 2023. Grounded-Segment-Anything.
- Cui, Y.; Chen, R.; Chu, W.; Chen, L.; Tian, D.; Li, Y.; and Cao, D. 2021. Deep learning for image and point cloud fusion in autonomous driving: A review. *IEEE Transactions on Intelligent Transportation Systems*, 23(2): 722–739.
- Fernandes, D.; Silva, A.; Névoa, R.; Simões, C.; Gonzalez, D.; Guevara, M.; Novais, P.; Monteiro, J.; and Melo-Pinto, P. 2021. Point-cloud based 3D object detection and classification methods for self-driving applications: A survey and taxonomy. *Information Fusion*, 68: 161–191.
- Fong, W. K.; Mohan, R.; Hurtado, J. V.; Zhou, L.; Caesar, H.; Beijbom, O.; and Valada, A. 2022. Panoptic nuscenes: A large-scale benchmark for lidar panoptic segmentation and tracking. *IEEE Robotics and Automation Letters*, 7(2): 3795–3802.
- French, G.; Laine, S.; Aila, T.; Mackiewicz, M.; and Finlayson, G. 2019. Semi-supervised semantic segmentation needs strong, varied perturbations. *arXiv preprint arXiv:1906.01916*.
- Geiger, A.; Lenz, P.; and Urtasun, R. 2012. Are we ready for autonomous driving? the kitti vision benchmark suite. In *2012 IEEE conference on computer vision and pattern recognition*, 3354–3361. IEEE.
- He, K.; Zhang, X.; Ren, S.; and Sun, J. 2016. Deep residual learning for image recognition. In *Proceedings of the IEEE conference on computer vision and pattern recognition*, 770–778.
- Hu, Q.; Yang, B.; Fang, G.; Guo, Y.; Leonardis, A.; Trigioli, N.; and Markham, A. 2022. Sqn: Weakly-supervised semantic segmentation of large-scale 3d point clouds. In *Computer Vision—ECCV 2022: 17th European Conference, Tel Aviv, Israel, October 23–27, 2022, Proceedings, Part XXVII*, 600–619. Springer.
- Jiang, L.; Shi, S.; Tian, Z.; Lai, X.; Liu, S.; Fu, C.-W.; and Jia, J. 2021. Guided point contrastive learning for semi-supervised point cloud semantic segmentation. In *Proceedings of the IEEE/CVF international conference on computer vision*, 6423–6432.
- Kirillov, A.; He, K.; Girshick, R.; Rother, C.; and Dollár, P. 2019. Panoptic segmentation. In *Proceedings of the IEEE/CVF Conference on Computer Vision and Pattern Recognition*, 9404–9413.
- Kirillov, A.; Mintun, E.; Ravi, N.; Mao, H.; Rolland, C.; Gustafson, L.; Xiao, T.; Whitehead, S.; Berg, A. C.; Lo, W.-Y.; et al. 2023. Segment anything. *arXiv preprint arXiv:2304.02643*.
- Kong, L.; Ren, J.; Pan, L.; and Liu, Z. 2023. Lasermix for semi-supervised lidar semantic segmentation. In *Proceedings of the IEEE/CVF Conference on Computer Vision and Pattern Recognition*.
- Li, J.; He, X.; Wen, Y.; Gao, Y.; Cheng, X.; and Zhang, D. 2022a. Panoptic-PHNet: Towards Real-Time and High-Precision LiDAR Panoptic Segmentation via Clustering Pseudo Heatmap. In *Proceedings of the IEEE/CVF Conference on Computer Vision and Pattern Recognition*, 11809–11818.
- Li, J.; and Lee, G. H. 2021. DeepI2P: Image-to-point cloud registration via deep classification. In *Proceedings of the IEEE/CVF Conference on Computer Vision and Pattern Recognition*, 15960–15969.
- Li, Y.; Ge, Z.; Yu, G.; Yang, J.; Wang, Z.; Shi, Y.; Sun, J.; and Li, Z. 2022b. Bevdepth: Acquisition of reliable depth for multi-view 3d object detection. *arXiv preprint arXiv:2206.10092*.
- Liang, T.; Xie, H.; Yu, K.; Xia, Z.; Lin, Z.; Wang, Y.; Tang, T.; Wang, B.; and Tang, Z. 2022. Bevfusion: A simple and robust lidar-camera fusion framework. *arXiv preprint arXiv:2205.13790*.
- Lin, Z.; Zhang, Z.; Chen, L.-Z.; Cheng, M.-M.; and Lu, S.-P. 2020. Interactive image segmentation with first click attention. In *Proceedings of the IEEE/CVF conference on computer vision and pattern recognition*, 13339–13348.
- Liu, Z.; Chen, H.; Feng, R.; Wu, S.; Ji, S.; Yang, B.; and Wang, X. 2021. Deep dual consecutive network for human pose estimation. In *Proceedings of the IEEE/CVF conference on computer vision and pattern recognition*, 525–534.

- Liu, Z.; Tang, H.; Amini, A.; Yang, X.; Mao, H.; Rus, D.; and Han, S. 2022. BEVFusion: Multi-Task Multi-Sensor Fusion with Unified Bird’s-Eye View Representation. *arXiv preprint arXiv:2205.13542*.
- Orsic, M.; Kreso, I.; Bevandic, P.; and Segvic, S. 2019. In defense of pre-trained imagenet architectures for real-time semantic segmentation of road-driving images. In *Proceedings of the IEEE/CVF Conference on Computer Vision and Pattern Recognition*, 12607–12616.
- Park, J.; Xu, C.; Zhou, Y.; Tomizuka, M.; and Zhan, W. 2022. Detmatch: Two teachers are better than one for joint 2d and 3d semi-supervised object detection. In *Computer Vision–ECCV 2022: 17th European Conference, Tel Aviv, Israel, October 23–27, 2022, Proceedings, Part X*, 370–389. Springer.
- Qi, C. R.; Su, H.; Mo, K.; and Guibas, L. J. 2017. Pointnet: Deep learning on point sets for 3d classification and segmentation. In *Proceedings of the IEEE conference on computer vision and pattern recognition*, 652–660.
- Radford, A.; Kim, J. W.; Hallacy, C.; Ramesh, A.; Goh, G.; Agarwal, S.; Sastry, G.; Askell, A.; Mishkin, P.; Clark, J.; et al. 2021. Learning transferable visual models from natural language supervision. In *International conference on machine learning*, 8748–8763. PMLR.
- Ramadan, H.; Lachqar, C.; and Tairi, H. 2020. A survey of recent interactive image segmentation methods. *Computational visual media*, 6: 355–384.
- Ren, S.; He, K.; Girshick, R.; and Sun, J. 2015. Faster r-cnn: Towards real-time object detection with region proposal networks. *Advances in neural information processing systems*, 28.
- Roriz, R.; Cabral, J.; and Gomes, T. 2021. Automotive LiDAR technology: A survey. *IEEE Transactions on Intelligent Transportation Systems*, 23(7): 6282–6297.
- Sindhwani, V.; Niyogi, P.; and Belkin, M. 2005. Beyond the point cloud: from transductive to semi-supervised learning. In *Proceedings of the 22nd international conference on Machine learning*, 824–831.
- Sofiuk, K.; Petrov, I. A.; and Konushin, A. 2022. Reviving iterative training with mask guidance for interactive segmentation. In *2022 IEEE International Conference on Image Processing (ICIP)*, 3141–3145. IEEE.
- Su, S.; Xu, J.; Wang, H.; Miao, Z.; Zhan, X.; Hao, D.; and Li, X. 2023. PUPS: Point Cloud Unified Panoptic Segmentation. *arXiv preprint arXiv:2302.06185*.
- Tan, X.; Ma, Q.; Gong, J.; Xu, J.; Zhang, Z.; Song, H.; Qu, Y.; Xie, Y.; and Ma, L. 2023. Positive-Negative Receptive Field Reasoning for Omni-Supervised 3D Segmentation. *IEEE Transactions on Pattern Analysis and Machine Intelligence*.
- Tarvainen, A.; and Valpola, H. 2017. Mean teachers are better role models: Weight-averaged consistency targets improve semi-supervised deep learning results. *Advances in neural information processing systems*, 30.
- Triess, L. T.; Dreissig, M.; Rist, C. B.; and Zöllner, J. M. 2021. A survey on deep domain adaptation for lidar perception. In *2021 IEEE Intelligent Vehicles Symposium Workshops (IV Workshops)*, 350–357. IEEE.
- Unal, O.; Dai, D.; and Van Gool, L. 2022. Scribble-supervised lidar semantic segmentation. In *Proceedings of the IEEE/CVF Conference on Computer Vision and Pattern Recognition*, 2697–2707.
- Wang, Q.; and Kim, M.-K. 2019. Applications of 3D point cloud data in the construction industry: A fifteen-year review from 2004 to 2018. *Advanced Engineering Informatics*, 39: 306–319.
- Xu, H.; Liu, F.; Zhou, Q.; Hao, J.; Cao, Z.; Feng, Z.; and Ma, L. 2021. Semi-supervised 3D object detection via adaptive pseudo-labeling. In *2021 IEEE International Conference on Image Processing (ICIP)*, 3183–3187. IEEE.
- Xu, X.; and Lee, G. H. 2020. Weakly supervised semantic point cloud segmentation: Towards 10x fewer labels. In *Proceedings of the IEEE/CVF conference on computer vision and pattern recognition*, 13706–13715.
- You, Y.; Phoo, C. P.; Luo, K.; Zhang, T.; Chao, W.-L.; Har-iharan, B.; Campbell, M.; and Weinberger, K. Q. 2022. Un-supervised Adaptation from Repeated Traversals for Autonomous Driving. *Advances in Neural Information Processing Systems*, 35: 27716–27729.
- Zhang, Z.; Zhang, Z.; Yu, Q.; Yi, R.; Xie, Y.; and Ma, L. 2023. LiDAR-Camera Panoptic Segmentation via Geometry-Consistent and Semantic-Aware Alignment. In *Proceedings of the IEEE/CVF International Conference on Computer Vision*, 3662–3671.
- Zhou, Z.; Zhang, Y.; and Foroosh, H. 2021. Panoptic-polarnet: Proposal-free lidar point cloud panoptic segmentation. In *Proceedings of the IEEE/CVF Conference on Computer Vision and Pattern Recognition*, 13194–13203.
- Zhu, X.; Zhou, H.; Wang, T.; Hong, F.; Ma, Y.; Li, W.; Li, H.; and Lin, D. 2021. Cylindrical and asymmetrical 3d convolution networks for lidar segmentation. In *Proceedings of the IEEE/CVF conference on computer vision and pattern recognition*, 9939–9948.
- Zou, Y.; Yu, Z.; Kumar, B.; and Wang, J. 2018. Unsupervised domain adaptation for semantic segmentation via class-balanced self-training. In *Proceedings of the European conference on computer vision (ECCV)*, 289–305.

Appendix

Detailed Experiments

Implementation Details

Point Cloud Panoptic Segmentation. Following the same configuration of Panoptic-PolarNet, the points among the area of $\{(x, y, z) \mid (3 \leq \sqrt{x^2 + y^2} \leq 50) \cap (-3 \leq z \leq 1.5)\}$ are voxelized with the grid size [480, 360, 32]. For Cylinder-Mix, the region size $[R_x, R_y, R_z] = [4, 4, 2]$. the weights of each term in loss $\mathcal{L}_{seg}, \mu_{hm} = 100, \mu_{os} = 10, \mu_{fm} = 1$. Besides, we set the learning rate at 0.002 and 0.004 for the datasets of SemanticKITTI and nuScenes, respectively. During the pretraining phase, as discussed in the *Self-Training* section of the paper, we configure 240, 300, 400, and 800 epochs for the experiments of semi-supervised ratios of 40%, 20%, 10%, and 1% on nuScenes. Similarly, for SemanticKITTI, we set 100, 180, 260, and 680 epochs for the corresponding SS ratios. While the epochs of the re-training phase are always 25.

Detection Network. The detector is trained on MMDetection (Chen et al. 2019) offline after generating and saving instance boxes in images by 3D-2D projection. We choose Faster R-CNN (Ren et al. 2015) as the backbone and train with a learning rate of 0.002 for SemanticKITTI and 0.005 for nuScenes images. Besides, we set 0.65 as the RPN threshold and 0.45 as the RCNN threshold. Fourth, infer image boxes from trained models, save these boxes, and wait for the fusion of SwiftNet.

Module Cost On nuScenes, the number parameters of baseline is 296.2MB, and the memory cost is 26.2GB (batch size=2). With Cylinder-Mix, the memory and time cost (1.2 seconds per frame) remain nearly unchanged. When the IPSL module is added, memory and time costs acceptably increase by 3.5GB and 0.13 seconds per frame, respectively.

Results of Detection Network

To evaluate the Detection Network, we present the metrics between the ground-truth bounding boxes projected from 3D points and the predicted ones. As shown in Table 6, Faster R-CNN (Ren et al. 2015) with ResNet-50 and ResNet-101 (He et al. 2016) are the models for the detector. There are the average precision (AP) of each *thing* class and mAP (%) on the kittiImages and nuImages, which refer to the camera images of SemanticKITTI and nuScenes, respectively. The mAP of the Detection Network on both datasets appears to be low, this is due to the imbalance in the number of instances and the confusion of semantics. Nevertheless, its AP could reach 65.9% if using a weighted sum by the number of instances. However, this also indicates the effectiveness of the IPSL module from another perspective. As these predicted instance boxes, as a form of weak labels, can still improve point cloud segmentation even without high precision.

Results of Segmentation on SemanticKITTI

As shown in table 1, we present the ablation results of the IPSL module and Cylinder-Mix components on SemanticKITTI. We observe that Cylinder-Mix performs well

Baseline	IPSL	CM	1%	10%	20%	40%
	✓		46.5	57.0	59.3	60.4
	✓	✓	46.9	57.9	59.8	60.7
	✓	✓	49.0	59.9	60.8	61.2

Table 1: Ablation experiments of the IPSL module and Cylinder-Mix on SemanticKITTI

Scope		1%	10%	20%	40%
total	baseline	46.5	57.0	59.3	60.4
	baseline + IPSL	46.9	57.9	59.8	60.7
inside	baseline	52.0	60.9	61.8	64.0
	baseline + IPSL	53.2	62.8	64.5	64.7

Table 2: Panoptic metrics on SemanticKITTI for total points and points inside the camera view.

on SemanticKITTI, particularly with improvements of 2.1% and 2% in PQ metric at 1% and 10% semi-supervised ratios, respectively. But the effect of the IPSL module is not as pronounced. With a specific comparison on the 20% SS ratio, Cylinder-Mix achieves a PQ gain of 2.1% on nuScenes in the paper, while the gain on SemanticKITTI is only 0.5%. It is probable that nuScenes has camera images with 6 views, which means that LiDAR-to-Camera projection and feature fusion of the IPSL module can cover most of the point cloud. In contrast, SemanticKITTI has only one front-facing camera, causing the IPSL module to affect a much smaller range of the point cloud, only 1/6 of the former.

Therefore, we introduce a new evaluation method for a fair comparison. To precisely assess the evaluation of IPSL on SemanticKITTI, we only calculate the PQ metrics for these points inside the camera view, cause IPSL primarily affects the points that can be projected onto the camera pixels. As shown in PQ metrics in Table 2, through limited gain from the IPSL module for all points, it shows a noticeable improvement for points within the camera’s field of view. This validates that IPSL primarily enhances the fusion of 2D-3D features and is actually effective.

Ablation of IPSL Module

Instance Heatmap Encoder Next, the parameters of the instance heatmap encoder have a direct impact on the heatmap, including P_{center} that affects the size of the instance centre heatmap and the radius of the corner points R_{corner} . We conduct ablation experiments with different settings of the two parameters on the 1% nuScenes. Also, we disable other data augmentation techniques to reduce model instability. As shown in Table 3, the experimental comparison is based on the performance of our baseline as setting 1, with a PQ of 47.0%. Firstly, compared to setting 1 and the others, the IPSL module is effective under most parameters. Secondly, by comparing experiments 2, 3, and 4, we find that a too-small radius of the centre heatmap with P_{center} is

setting	R_{corner}	P_{center}	PQ
1	/	/	47.0
2	5	1/4	48.5
3	5	1/3	48.1
4	5	1/10	47.9
5	10	1/4	48.2

Table 3: Ablation study on boxes heatmap

	p_{cylmix}	$[R_x, R_y, R_z]$	PQ
baseline + IPSL	0	/	46.5
LaserMix	0.25	/	47.0
Cylinder-Mix	1	[4,4,2]	47.5
	0.5	[4,4,2]	47.4
	0.25	[4,4,2]	49.0
	0.25	[2,2,1]	46.9
	0.25	[16,16,4]	47.9
	0.25	[1,1,4]	47.0
	0.25	[8,8,1]	47.1

Table 4: Ablation of Cylinder-Mix on 1% SemanticKITTI

not conducive to indicating instance size information, and a parameter of $P_{center} = 1/4$ is a good choice, resulting in a PQ of 48.5%. Finally, by comparing experiments 2 and 5, we conclude that a too-large radius of the corner heatmap can decrease PQ, possibly because it causes confusion in indicating instance information.

Ablation of Cylinder-Mix

As shown in the table 4, to explore the optimal parameters for using Cylinder-Mix(CM), we conducted ablation experiments on the mixing probability p_{cylmix} and region size $[R_x, R_y, R_z]$ in SemanticKITTI. We choose 1% as semi-supervised ratio, cause Cylinder-Mix is sensitive at this setting to distinguish effects in PQ under different parameters and the experimental comparison is based on the baseline with the IPSL module as a reference.

Firstly, to make a fair comparison with Lasermix, ring-mixing in Lasermix is performed as data augmentation on our baseline instead of Cylinder-Mix. At 25%, LaserMix has a PQ of 47.0%, while CM can achieve a maximum PQ of 49.0%. Secondly, we fix the region size to [4,4,2] and adjusted the p_{cylmix} . The results demonstrate that $p_{cylmix} = 1$ is not absolutely optimal and the model tends to benefit more from partially mixed data with original data rather than entirely mixed data. Finally, we fixed the p_{cylmix} to 25% and adjusted the region size to [4,4,2], [16,16,4], [1,1,4] and [8,8,1], respectively. It is expected to evaluate the sensitivity of Cylinder-Mix along with the Z-axis and X-Y axes. We don't separately increase the region size of the X and Y axes because they are equivalent in the cylinder voxel. Based on the experimental results, we draw the conclusion that adding region size solely at R_z or the XY-plane is not the optimal mixing strategy, and too few regions to mix are also not ideal. A moderately large region size, such as [4,4,2], is a good choice of region size.

		nuScenes	SemanticKITTI
PQ	w/o IB	75.4	59.1
	baseline	77.6	59.8
mIoU	w/o IB	77.9	63.7
	baseline	80.7	64.2

Table 5: Ablation study of RGB information on fully supervised dataset. w/o IB: baseline without Image Branch.



Figure 1: Ground truth and high-quality GSA mask.

Supplementary Experiments

Improvement of RGB images

For RGB information, we removed the image branch of our baseline to observe its contribution on the fully supervised datasets. As shown in Table 5, the RGB information results in a PQ gain of 2.1% and an mIoU gain of 2.9% on nuScenes. However, the improvement is not significant on the SemanticKITTI, it may be attributed to the fact that SemanticKITTI has only 1/6th of the angle of camera view compared to nuScenes.

Details PQ and IoU scores

In Table 7, we present the class-wise IoU and PQ on the val set of the SemanticKITTI under the 100% and 10% settings. The table indicates that our model does not show significant improvements in the *stuff* category, but shows a clear increase in PQ for the *thing* category, which indicates that the proposed IPSL module and Cylinder-Mix put more emphasis on segmentation of *thing* classes.

Visualization

SAM mask

For each frame of the camera image, we enter each category name of the dataset as prompt. With SAM masks (Grounded Segment Anything, GSA shown in Figure 1), our approach achieves very close performance 70.7@mIoU compared with the detector 70.9@mIoU in Table 4 of original paper. That demonstrates IPSL is able to combine with vision foundation model.

segmentation visualization of point clouds

As shown in Figure 2, we provide visualizations of point clouds for the ground truth, predictions of the baseline, and our model. The color red is used to indicate incorrect predictions in the point cloud. Semantic segmentation and instance segmentation visualisations are presented. The mIoU or PQ excluding categories that are absent within ground truth is labeled in the bottom-right corner of the subplot. The 100% on the left indicates the model trained on the full SemanticKITTI dataset, while the 10% on the right means only using on 10% labeled subset following our SS setting.

kittiImages	car	bicycle	truck	person	motorcyclist	bicyclist	motor-cycelle	other-vehicle	sum or mAP	weighted mAP		
Number of instances	36115	2602	258	3334	130	1488	897	2230	43927			
Faster R-CNN + ResNet-50	69.7	16.4	14.4	28.2	0.1	52.8	17.7	21.4	27.5	63.7		
Faster R-CNN + ResNet-101	71.4	21	20.6	27.8	0	56.8	21.3	27.5	30.8	65.9		
nulImages	car	bicycle	truck	pedestrian	motor-cycle	bus	barrier	construction vehicle	trailer	traffic cone	sum or mAP	weighted mAP
Number of instances	70398	2201	16407	33180	2440	3449	25059	2716	4451	12892	160301	
Faster R-CNN + ResNet-50	44.6	21.7	39.2	25.5	26.9	54.3	33.6	15.2	27.8	17.5	30.6	38.4
Faster R-CNN + ResNet-101	45	21.3	40.3	25.6	27.6	55.4	34.3	16.7	28.5	17.4	31.2	38.9

Table 6: Results on Detection Network of different backbone

		metrics	car	bicy	moto	truck	bus	bus	ped	b.cyc	PQ.th	road	park	walk	o.gro	build	fence	veg	trunk	terr	pole	sign	PQ.st	mean
100%	baseline	IoU	94.1	54.71	72.55	75.01	45.98	72.31	84.78	29.09	66.07	94.32	44.59	80.82	3.02	88.49	45.79	85.83	64.57	69.58	65.5	47.81	62.76	64.15
		PQ	90.29	58.05	70.63	57.79	48.44	80.02	87.82	35.05	66.01	94.26	23.71	77.48	0.13	86.92	16.75	83.54	49.3	55.79	61.57	58.16	55.238	59.77
	ourmodel	IoU	94.37	57.46	73.93	76.36	59.11	76.37	88.17	26.07	68.98	93.5	39.65	80.33	2	89.44	51.21	85.79	65.12	69.73	65.4	47.27	62.68	65.33
		PQ	90.38	60.53	74.80	62.10	58.33	82.85	89.49	31.36	68.73	93.74	22.10	77.46	0	87.04	19.95	84.23	49.62	54.23	60.92	56.18	55.04	60.81
10%	baseline	IoU	92.5	50.96	60.66	73.77	39.38	69.01	78.74	12.76	59.72	94.15	43.46	80.79	2.59	89.71	52.26	86.54	64.85	70.49	66.24	45.47	63.32	61.81
		PQ	88.26	52.36	64.19	46.19	42.19	76.25	87.75	19.71	59.61	93.97	22.27	76.81	0.13	86.87	19.28	84.93	49.63	54.84	62.17	54.72	55.06	56.98
	ourmodel	IoU	94.21	54.66	68.19	76.08	49.83	73.28	83.19	26.19	65.70	94.64	43.43	81.43	0.41	90.75	52.17	87.58	66.67	72.63	66.48	48.44	64.06	64.75
		PQ	89.68	56.15	71.20	55.63	50.19	80.82	87.86	27.96	64.94	94.56	25.46	77.96	0.46	87.93	19.16	85.32	52.16	55.37	61.68	57.80	56.17	59.86

Table 7: Class-wise IoU and PQ scores on the val set of SemanticKITTI.

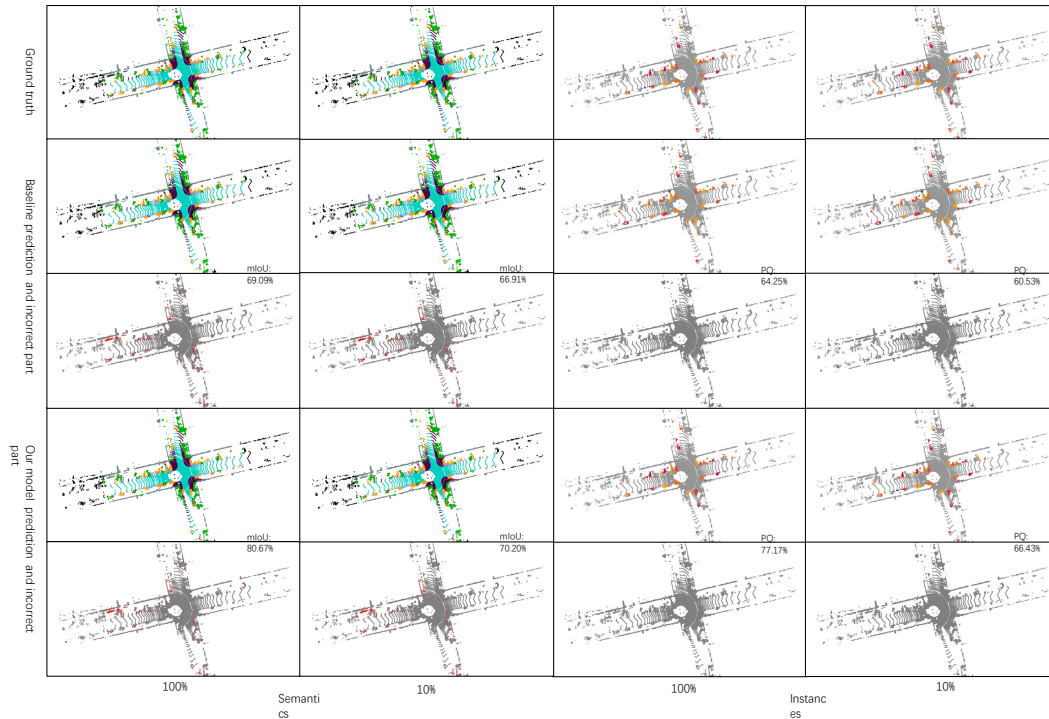


Figure 2: Visualization on SemanticKITTI